Perchloroethylene gas-phase degradation over titania-coated transparent monoliths

Filipe V.S. Lopes[a], Sandra M. Miranda[a,b], Ricardo A.R. Monteiro[a], Susana D.S. Martins[c], Adrián M.T. Silva[b,*], Joaquim L. Faria[b], Rui A.R. Boaventura[a], Vítor J.P. Vilar[a,*]

[a] LSRE – Laboratory of Separation and Reaction Engineering, Associate Laboratory LSRE/LCM, Faculdade de Engenharia, Universidade do Porto, Rua Dr. Roberto Frias, 4200-465 Porto, Portugal
[b] LCM – Laboratory of Catalysis and Materials, Associate Laboratory LSRE/LCM, Faculdade de Engenharia, Universidade do Porto, Rua Dr. Roberto Frias, 4200-465 Porto, Portugal
[c] IDMEC – Institute of Mechanical Engineering, Faculdade de Engenharia, Universidade do Porto, Rua Dr. Roberto Frias, 4200-465 Porto, Portugal

A R T I C L E   I N F O

A B S T R A C T

Perchloroethylene (PCE) has been detected as one of the major pollutants in indoor air of wastewater treatment plants (WWTPs) with closed facilities. Its hazardousness requires the complete PCE removal from air. For this reason, gas-phase photooxidation of PCE was studied in a continuous-flow tubular photoreactor under simulated solar radiation. Since negligible degradation of PCE was observed by photolysis, photocatalytic oxidation (PCO) experiments were carried out employing a catalytic bed of cellulose acetate monoliths (CAM) coated with TiO$_2$ (TiO$_2$-CAM). The three TiO$_2$-CAM samples tested (3, 6, and 9 TiO$_2$ dip-coating layers), showed that the catalytic activity increases considerably with the number of layers (~92% for the 9-layered TiO$_2$-CAM). Different conditions of feed flow rate, pollutant concentration, feed relative humidity, and incident irradiance were tested for the 9-layered TiO$_2$-CAM photocatalyst in order to assess the most relevant operating parameters. Taking into consideration the small path of the photoreactor employed (0.16 m length), PCO of PCE showed interesting results, achieving degradation efficiencies between 90 and ~98%, depending on the operating conditions used. The mathematical modelling of PCE kinetics through PCO suggested that there is no competition between PCE and H$_2$O molecules to the surface active sites, even considering them as independent molecules that target distinct surface active sites (Langmuir–Hinshelwood bimolecular competitive two types of sites rate model). The validation of the PCO mathematical model at lab-scale allowed predictive simulations for PCO of PCE that can be used for possible scale-up a unit aiming at completely mineralization of PCE under solar irradiation. Finally, identification of PCE by-products allowed the complete formulation of a feasible reaction mechanism.

© 2013 Elsevier B.V. All rights reserved.

1. Introduction

Volatile organic compounds (VOCs) represent a very active group of pollutants present in water and air, emitted into the atmosphere by human and industrial activities, such as fuel combustion, residential solvent, paint application, among several others [1–5]. Wastewater treatment plants (WWTPs) with opened or closed facilities are also a significant source of VOCs. After performing three air sampling campaigns in a WWTP located in North of Portugal, Teixeira et al. [6] reported a wide range of VOCs in different sites of the WWTP being PCE one of the more representative

pollutants. PCE has been used as model pollutant in different photocatalytic studies since it has been considered a priority pollutant (due to its toxicity and suspected carcinogenicity to human health) [7,8].

Photocatalytic oxidation processes (PCO) have demonstrated to be an attractive and promising approach technology for air purification [1,2]. For gas-phase PCO treatment, the use of photocatalytic powders (commonly used in water detoxification) is mostly avoided due to fluidization and separation problems and ineffective catalyst surface irradiation ("shading effect") [9–12]. In this context, immobilized catalysts offer a simple and practicable solution, in particular for bed packing photoreactors [9,13,14]. Different techniques have been suggested for catalyst thin-film immobilization, namely, spray pyrolysis, chemical or physical vapour deposition, sputtering, dip-coating including also sol–gel methods, among

Nomenclature

Latin letters

$C_{\text{C-PCE,Feed}}$	carbon atoms concentration of PCE on the feed stream [ppm]
C_i	gas phase concentration of compound i [ppm]
$C_{i,\text{C-PCE}}$	carbon atoms concentration of compound i formed by PCE degradation [ppm]
$C_{i,\text{Feed}}$	gas phase concentration of component i on the feed stream [ppm]
C_{PCE}	gas phase concentration of PCE [ppm]
$C_{\text{H}_2\text{O}}$	gas phase concentration of H_2O [ppm]
$C_{\text{PCE,Exit}}$	gas phase concentration of PCE on the exit stream [ppm]
$C_{\text{PCE,Feed}}$	gas phase concentration of PCE on the feed stream [ppm]
d_{ch}	characteristic length of the monolithic channel (hole width) [m]
$d_{\text{in,e}}$	external diameter of the glass and quartz inner tubes [mm]
$d_{\text{in,i}}$	internal diameter of the glass and quartz inner tubes [mm]
$d_{\text{ot,e}}$	external diameter of the Pyrex-glass outer tube [mm]
$d_{\text{ot,i}}$	internal diameter of the Pyrex-glass outer tube [mm]
D_{ax}	axial dispersion coefficient [m^2 s^{-1}]
D_{m}	molecular diffusivity of the feed mixture [m^2 s^{-1}]
$e_{\text{w,ch}}$	wall thickness of the monolithic channel [m]
I	incident irradiance [W m^{-2}]
k	reaction rate constant [mol m^{-2} s^{-1} W^{-1} m^2]
k_{B}	Boltzmann's constant [J K^{-1}]
$K_{\text{H}_2\text{O}}$	H_2O adsorption equilibrium constant in a single site [M^{-1}]
$K_{\text{H}_2\text{O,1}}$	H_2O adsorption equilibrium constant on two types of sites (site 1) [M^{-1}]
$K_{\text{H}_2\text{O,2}}$	H_2O adsorption equilibrium constant on two types of sites (site 2) [M^{-1}]
K_{PCE}	PCE adsorption equilibrium constant in a single site [M^{-1}]
$K_{\text{PCE,1}}$	PCE adsorption equilibrium constant on two types of sites (site 1) [M^{-1}]
$K_{\text{PCE,2}}$	PCE adsorption equilibrium constant on two types of sites (site 2) [M^{-1}]
L_{CAM}	length of the cellulose acetate monolith [mm]
L_{in}	length of the Pyrex-glass inner tube [mm]
L_{ot}	length of the Pyrex-glass outer tube [mm]
L_{R}	length of the photocatalytic bed [mm]
m_{CAM}	mass of cellulose acetate monoliths [g]
m_{TiO_2}	mass of catalyst deposited on each monolith [g]
$M_{\text{C atom}}$	molecular weight of a carbon atom [g mol^{-1}]
M_i	molecular weight of compound i [g mol^{-1}]
n_{layers}	number of TiO$_2$ layers deposited on CAM
$(N_{\text{C atom}})|_i$	number of carbon atoms of each component i molecule
P	pressure [Pa]
Q_{Feed}	total feed flow rate [mL min^{-1}]
RH_{Feed}	relative humidity of the feed stream (water vapour content) [%]
r	degradation rate [mol s^{-1} m^{-2}]
r_{PCE}	degradation rate of PCE [mol s^{-1} m^{-2}]
R^2	squared correlation coefficient
S_{R}^2	sum of squared residuals between experimental and calculated rates [mol^2 m^{-4} s^{-2}]
t	time [s]
T	temperature [K]
$\bar{u}_{0,\text{ch}}$	superficial velocity in the monolithic channels [m s^{-1}]
V_{R}	volume of photocatalytic bed [mm^3]
z	partition of the photocatalytic bed length (L_{R} in m) [m]

Greek letters

ε	photocatalytic bed porosity
$\varepsilon_i/k_{\text{B}}$	Lennard–Jones parameter: compound i maximum energy of interaction between molecular pairs (K)
$\eta_{\text{Mineralization}}$	mineralization efficiency [%]
λ	UV/vis wavelength [nm]
ρ_{CAM}	cellulose acetate monoliths' density [g cm^{-3}]
ρ_{TiO_2}	catalyst density [g cm^{-3}]
σ_i	Lennard–Jones parameter: collision molecular diameter of compound i [Å]
ν_i	stoichiometric coefficient of compound i in the overall reaction

others [15–19]. Because of its simplicity and low associated synthesis costs, dip-coating is a suitable methodology for the production of catalytic films. Nevertheless, working conditions should be carefully selected in order to avoid undesired film cracking (resulting in the catalyst layer delamination) [15]. An essential parameter in the synthesis of thin-films is the number of dip-coating layers, i.e., number of depositions in the same support surface: photocatalytic activity increases with the growth of film thickness (till a certain point); on the other hand, increasing the number of layers, fabrication costs also increase [20,21].

Support material selection is another import feature in gas-phase PCO as it directly affects the catalyst activity, homogeneity, and adhesion to its surface [15]. The support should be transparent to UV radiation (allowing photo-activation of the whole coating), resistant to photooxidation (avoiding both transparency and mechanical resistance reduction), adequate to obtain low pressure drop and reduced mass transport limitations, and should also acts as pollutant–catalyst contact promoter (i.e., allowing reduced residence time by providing enough available catalytic sites) [9–13,22–24]. Several supports have been employed for photocatalytic applications, such as ceramic tiles, glass tubes, rods, or spheres, fibreglass, paper, stainless steel, and monolithic ceramics or transparent polymers. However, only the transparent polymeric monoliths (low-cost, lightweight and easily shaped transparent solid structures with open-ended parallel channels) assemble all the above desirable features [9,13–15,22,25,26]. Thus, monolithic supports, such as thin-walled honeycomb structures of cellulose acetate, are extremely suitable for purification of large volumes of contaminated air, at different continuous feed stream conditions, and for fast and efficient gas-phase degradation of pollutants, attaining high process efficiencies [9,13,14,22].

In this context, titanium dioxide (TiO$_2$) thin-films supported on cellulose acetate monoliths (CAM) were prepared for PCE photocatalytic degradation under simulated solar irradiation. A lab-scale continuous-flow tubular photoreactor was employed in photooxidation experiments in order to evaluate the practicable use and efficiency of TiO$_2$-based monolithic catalysts. Aiming a catalyst efficiency enhancement for this particular application, the effect of different multi-layered TiO$_2$ cellulose acetate monoliths on the photocatalytic activity was assessed. For the most efficient samples, PCO of PCE was evaluated as a function of feed flow rate, PCE concentration, feed relative humidity, and incident
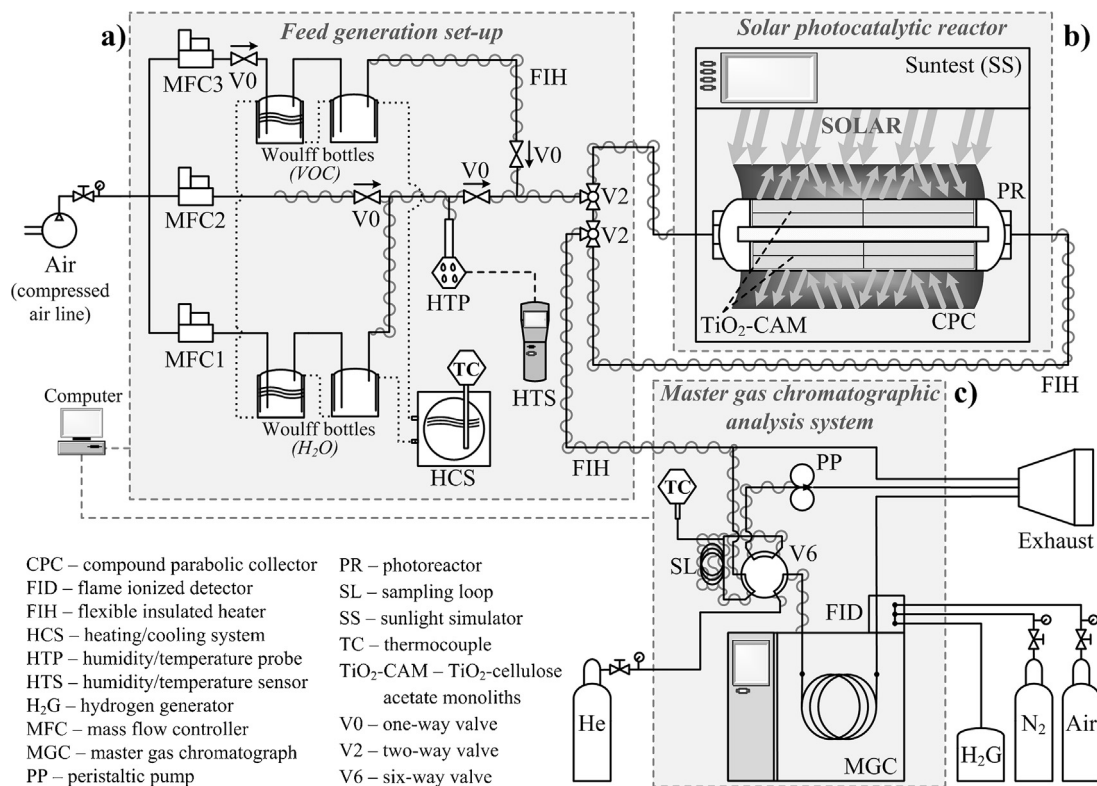
Fig. 1. Schematic representation of the experimental set-up: (a) lab-scale unit used for the generation of air streams containing PCE and water vapour; (b) continuous-flow tubular photoreactor placed in the sunlight simulator; (c) master gas chromatographic analysis system used for the analysis of the photoreactor feed and exit streams. Reprinted (adapted) with permission from Lopes et al. [28]. Copyright © 2012, Elsevier.

irradiance. Additionally, combining a complete mathematical model with different kinetic rate expressions, the kinetics through PCO was studied. Finally, after identification and quantification of the PCE by-products, a complete reaction mechanism was suggested.

2. Experimental

2.1. Materials and chemicals

Nitric acid (HNO_3; 65%, Merck S.A.), titanium (IV) isopropoxide (TIP: $Ti(iOPr)_4$; 97%, Sigma–Aldrich Co. LLC.), and Triton™ X-100 (t-Oct-C_6H_4-$(OCH_2CH_2)_nOH$, $n = 9$–10, Sigma–Aldrich Co. LLC.) were used in the preparation of titanium dioxide (TiO_2) sol; a cellulose membrane (Spectra/Por® Dialysis Membrane 3500 MWCO, Spectrum Laboratories, Inc.) was employed in the final sol dialysis. Cellulose acetate monoliths (CAM: TIMax CA50-9/S–L_{CAM} = 80 mm, d_{ch}^2 = 9 mm × 9 mm, $e_{w,ch}$ = 0.1 mm; Wacotech GmbH & Co. K.) were used as support of the catalytic film. For the generation of contaminated air streams with water vapour content, perchloroethylene (PCE; 99.5%–HCl: <0.005%, H_2O: <0.02%, non-volatile matter: <0.005%; Panreac Química S.A.U.), ultrapure water, and deionized water were used without further purification. Air Liquide provided all gases, each one with a minimum total purity of 99.999%: helium N50, nitrogen N50, and air K N50 (O_2: 20 ± 1%; H_2O: <3 ppm; C_nH_m: <0.1 ppm; CO_2: <1 ppm; CO: <1 ppm).

2.2. Catalyst preparation and characterization

TiO_2 thin-films were prepared/supported on CAM samples by combining the sol–gel and dip-coating methods [27], resulting in TiO_2-supported cellulose acetate monoliths (named as TiO_2-CAM). Before coating, the substrate samples were soaked during 1 h with

distilled water containing an anionic detergent (Extran, Merck S.A.) and subsequently washed exhaustively with Milli-Q water. Finally, CAM samples were heated up to 323 K to dryness. TIP was the precursor employed as TiO_2 source and it was added to an aqueous solution of nitric acid (74:900:6.5, v/v/v of TIP, H_2O, and HNO_3); this solution was stirred until complete peptization under magnetic stirring at ~298 K. The final sol was dialyzed in a cellulose membrane to a final pH of 3.0. All preparation steps at room temperature (~298 K). Several layers were deposited by dip-coating (Dip-Coater RDC21-K, Bungard Elektronik GmbH & Co. KG.) at a withdrawal

Table 1
Photoreactor tubes dimensions employed in the gas-phase PCO of PCE under simulated solar irradiation; catalytic bed characteristics used in the PCE photocatalytic experiments.

		Photoreactor		
Outer tube (Pyrex-glass tube)	L_{ot} [cm]	16.0		
	$d_{ot,e}$ [cm]	5.00		
	$d_{ot,i}$ [cm]	4.64		
Inner tube (soda-lime glass tube)	L_{in} [cm]	16.0		
	$d_{in,e}$ [cm]	2.00		
	$d_{in,i}$ [cm]	1.64		
		Catalytic bed		
Photocatalytic bed (TiO_2-CAM)	L_R [cm]	16.0		
	V_R [cm³]	2.2×10^2		
	ε	0.989		
	n_{layers}	3	6	9
TiO_2 thin-films	m_{TiO_2} [g]	0.0545	0.0893	0.1254
	ρ_{TiO_2} [g cm⁻³]	2.61		
Cellulose acetate monoliths (CAM)	m_{CAM} [g]	3.273	3.232	3.118
	ρ_{CAM} [g cm⁻³]	1.30		
	d_{ch} [cm]	0.9		

List of abbreviations:
CPC – compound parabolic collector
FID – flame ionized detector
FIH – flexible insulated heater
HCS – heating/cooling system
HTP – humidity/temperature probe
HTS – humidity/temperature sensor
H_2G – hydrogen generator
MFC – mass flow controller
MGC – master gas chromatograph
PP – peristaltic pump
PR – photoreactor
SL – sampling loop
SS – sunlight simulator
TC – thermocouple
TiO_2-CAM – TiO_2-cellulose acetate monoliths
V0 – one-way valve
V2 – two-way valve
V6 – six-way valve

Table 2
Experimental conditions employed in gas-phase TiO$_2$-CAM PCO of PCE carried out in a continuous-flow tubular photoreactor under different simulated solar irradiations.

Run	Q_{Feed} [mL min^{-1}][c]	$C_{PCE,Feed}$ [ppm]	RH_{Feed} [%][c]	I [W m^{-2}][d]
1[a,b]	150	945	30	38.4
2[a,b]	150	945	30	29.1
3[a,b]	150	945	30	18.9
4[a]	75	945	30	38.4
5[a]	75	945	30	29.1
6[a]	75	945	30	18.9
7[a]	300	945	30	38.4
8[a]	300	945	30	29.1
9[a]	300	945	30	18.9
10[a]	150	296	30	38.4
11[a]	150	296	30	29.1
12[a]	150	296	30	18.9
13[a]	150	535	30	38.4
14[a]	150	535	30	29.1
15[a]	150	535	30	18.9
16[a]	150	1633	30	38.4
17[a]	150	1633	30	29.1
18[a]	150	1633	30	18.9
19[a]	150	945	8	38.4
20[a]	150	945	8	29.1
21[a]	150	945	8	18.9
		$T = 298$ K; $P = 1$ bar		

[a] Experimental conditions employed in PCO of PCE with 9-layered TiO$_2$-CAM.
[b] Experimental conditions employed in PCO of PCE with 3- and 6-layered TiO$_2$-CAM.
[c] Measured at 298 K and 1 bar.
[d] Measured within 280–400 nm (sunlight UV fraction).

rate of 0.8 mm s^{-1} on CAM. After applying each layer, monoliths were dried at 323 K for 1 h, finally the materials were rinsed three times with ultrapure water and dried at 323 K for 2 h. As result, three sets of TiO$_2$-CAM were produced with deposition on CAM of 3, 6, and 9 TiO$_2$ layers, respectively. Finally, monoliths coated with TiO$_2$ were packed into a lab-scale continuous-flow tubular photocatalytic reactor (see Section 2.4) for the study of PCE degradation through PCO. Note that, CAM supports are thermally sensitive substrates (above 418 K [9]), thus the high treatment temperatures typically used for TiO$_2$ calcination ($\sim$723 K) and formation of well-crystallized TiO$_2$ particles, are not compatible with the employed support [13]; however, the TiO$_2$ sols prepared by this method are crystalline enough to display photocatalytic activity.

The surface morphology of the catalyst film samples and their chemical composition were characterized by scanning electron microscopy (SEM) coupled with energy dispersive X-ray (EDX) analysis, using a FEI Quanta 400 FEG ESEM/EDAX Genesis X4 M apparatus equipped with a Schottky field emission gun (for optimal spatial resolution). The TiO$_2$-CAM samples were mounted on a double-sided adhesive tape made of carbon and observed at different magnifications (the cross-section of the catalyst films was also measured by this technique). These SEM/EDX analyses were made at CEMUP (Centro de Materiais da Universidade do Porto). X-ray diffraction (XRD) analysis was performed in a PAN'alytical X'Pert MPD equipped with a X'Celerator detector and secondary monochromator (Cu Kα, $\lambda = 0.154$ nm, 50 kV, 40 mA; data recorded at a 0.017° step size). Rietveld refinement with PowderCell software was used to identify the crystallographic phases present and to calculate the crystallite size from the XRD diffraction patterns. This method employs a modified version of the Debye–Scherrer equation to simultaneously determine the crystallite size and non-uniform strain.

2.3. Feed generator

Air streams containing PCE and water vapour were generated using an in-house lab-scale facility (schematically shown in Fig. 1a)
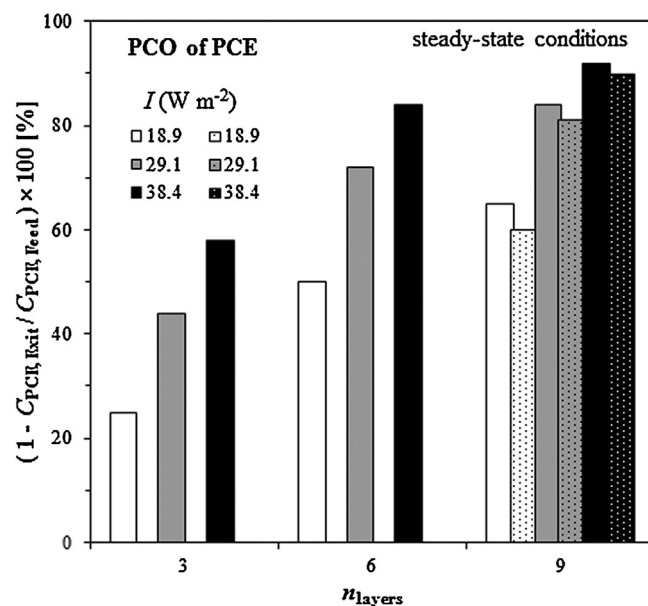

Fig. 2. Effect on photocatalytic efficiency (at steady-state conditions) for different number of TiO$_2$ layers deposited on CAM [n_{layers}]: incident irradiances measured within 280–400 nm (sunlight UV fraction) of 18.9 (white), 29.1 (grey), and 38.4 W m^{-2} (black); layered TiO$_2$-CAM first use (full-coloured column) and after more than 50 h under simulated solar irradiation and continuous feeding for the 9-layered TiO$_2$-CAM sample (dotted columns); $C_{PCE,Feed} = 945$ ppm, Q_{Feed}[a] $= 150$ mL min^{-1}, RH_{Feed}[a] $= 30$%, and $T = 298$ K; operation conditions reported in Table 2 (runs 1–3) ([a]measured at 298 K and 1 bar).

[28]. Three mass flow controllers (El-Flow, Bronkhorst High-Tech B.V.) allow the generation of air streams containing different PCE and water vapour concentrations by flowing air through Woulff bottles (supplied by Normax, Lda) filled with pure PCE liquid solution and deionized water. A relative humidity/temperature probe connected to a data logger (9735/635-2, Testo) was used to read both relative humidity and temperature of the contaminated air stream. The PCE and water vapour contents were fixed as a result of controlling the flow rate of the air stream and its temperature, using a temperature controlling system (thermostatic bath GD100 R2, Grant Instruments). To avoid pollutant/water condensation, the 1/4 in. stainless steel tubing was covered with a flexible insulated heater, capable of heat up to 423 K.

2.4. Lab-scale photoreactor

A lab-scale continuous-flow tubular photoreactor was employed in the study of gas-phase PCO of PCE (see Fig. 1b) [28]. It is mainly composed by two concentric glass tubes: an outer tube of Pyrex-glass (Duran borosilicate glass 3.3, Schott-Rohrglas GmbH) and an inner tube of soda-lime glass (Linex) centred in the axial position, allowing the penetration of simulated solar radiation through their structures. The photocatalytic fixed-bed of TiO$_2$-CAM was located filling the void between these tubes. The photoreactor has four equidistant inlets to ensure a better distribution of the feed stream throughout the bed. Table 1 presents the tubes dimensions and catalytic bed characteristics. An Atlas Suntest XLS+ unit (Atlas Material Testing Technology GmbH) was used to simulate solar radiation. This equipment can simulate the spectral distribution of global solar radiation in the UV and visible wavelength range (300 nm < λ < 800 nm). The irradiance amplitude of the lamp is between 250 and 500 W m^{-2} and the incident irradiance on the catalyst surface was measured with a broadband UV radiometer (CUV 5, Kipp & Zonen B.V.), placed on the outside of the outer tube and at the same height (distance
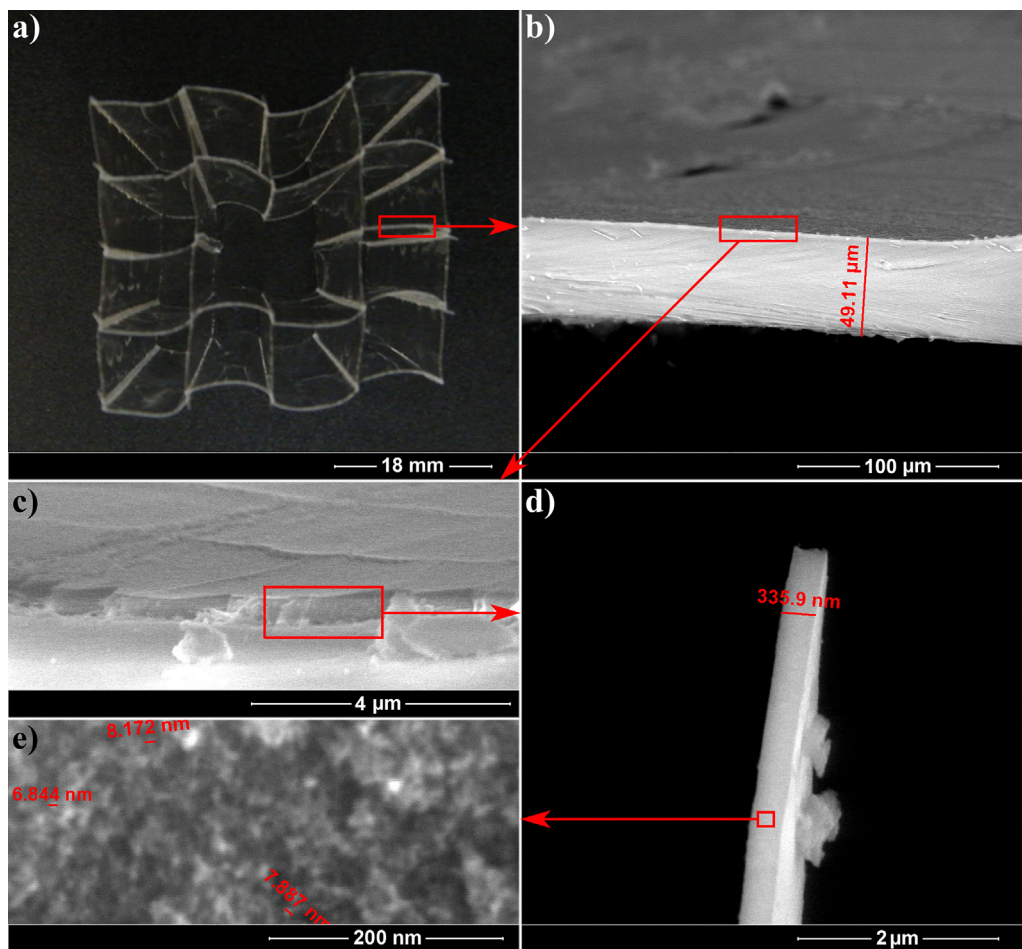
Fig. 3. Photograph (a) and SEM micrographs (b–d) of 9–layered TiO_2-CAM used in PCO of PCE.

to the radiation source), within a spectral range of 280–400 nm (UV fraction of the incident solar light). Despite the reflector system in the solar simulator bed tray, the photoreactor is placed in the top of a reflective surface of anodized aluminium (named compound parabolic collector – CPC) to avoid the loss of a large amount of radiation and to uniform the irradiance on the catalytic bed.

2.5. Photoreactor feed and exit stream analysis

A master gas chromatographic analysis system (MGC Fast GC, Dani Instruments S.p.A.), with a coupled two-position valve for sampling storage, was used for further PCE concentration analysis through a flame ionization detector (FID) (see Fig. 1c) [28]. A peristaltic pump (313F, Watson-Marlow Pumps Group), placed at the end of the line, was employed to ensure that the loop of the two-position valve is completely filled with the gas sample. VOCs by-products were also analyzed at steady-state, sampling the photoreactor exit stream to a Tedlar bag (232-05SKC, SKC, Inc.) and then transferring the sample to stainless steel tubes with Tenax TA60/80 mesh (Supelco, Sigma–Aldrich Co. LLC.). After sampling, VOC identification and quantification were performed with a thermal desorption system (SDT 33.50, Dani Instruments S.p.A.) working on line with the GC/MSD device (a gas chromatograph GC 6890N coupled to a mass spectrometer detector MSD 5973, Agilent Technologies, Inc.). The response factor of toluene (ISO 16000-6 [29]) was used to determine the concentration of the major
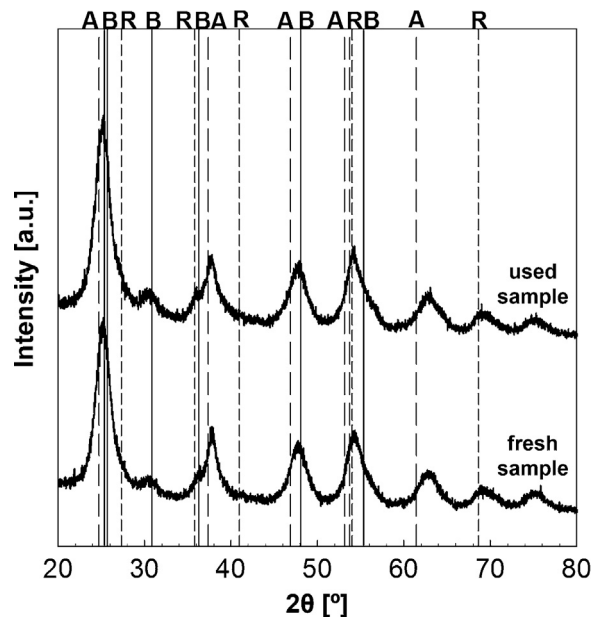

Fig. 4. XRD patterns of the TiO_2 powder before (fresh sample) and after 50 h+ of use in PCO of PCE (used sample); A, B, and R refers to anatase, brookite, and rutile TiO_2 crystalline phases, respectively.
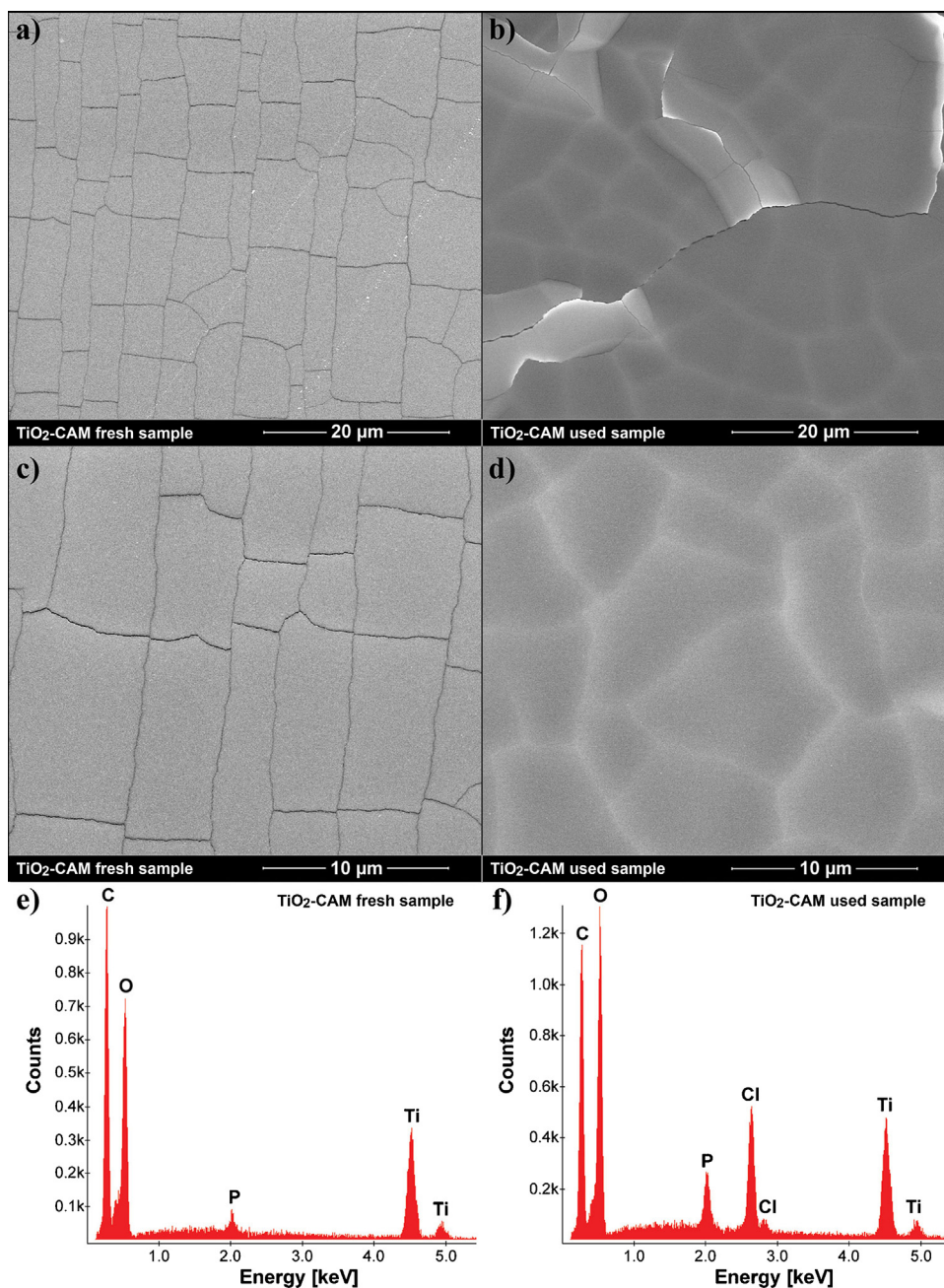
Fig. 5. SEM micrographs (a–d) and EDX spectra (e and f) of 9-layered TiO_2-CAM before (left-side images) and after 50 h+ of use (right-side images) in PCO of PCE.

products (for PCE and trichloroethylene, specific response factors were used).

2.6. Solar photochemical and photocatalytic oxidation of PCE

In order to study the PCE photochemical oxidation, the continuous-flow photoreactor was initially assembled without TiO_2-CAM (catalytic bed). PCO of PCE under simulated solar irradiation was performed employing three different photocatalytic beds of layered TiO_2-CAM samples (3, 6 and 9 layers). Then, using the samples with the number of dip-coating layers that presents the higher photocatalytic efficiency, PCE conversion in PCO was evaluated for several experimental conditions of the feed stream: (a) different flow rates (75–300 mL min^{-1}, measured at 1 bar and 298 K); (b) PCE concentrations (300–1600 ppm); (c)

relative humidities (8–30%, measured at 1 bar and 298 K). Additionally, different incident irradiances were employed for each experimental condition (18.9–38.4 W m^{-2}, measured within 280–400 nm: UV fraction of the incident sunlight). Table 2 reports the experimental conditions employed within this work. Activation and degassing of the catalytic bed was performed overnight, before all experiments, using a humid air (40%) stream with a total flow rate of 30 mL min^{-1} (measured at 1 bar and 298 K). Before turning on illumination in the solar simulator, the catalytic bed was continuously fed; several outlet stream samples were analyzed to verify the feed composition steadiness. Finally, at steady-state conditions, the PCE degradation efficiency was determined for each experiment: $C_{PCE,Exit}/C_{PCE,Feed}$, where $C_{PCE,Feed}$ (mol m^{-3}) and $C_{PCE,Exit}$ (mol m^{-3}) being the PCE concentrations on the feed and exit streams, respectively.
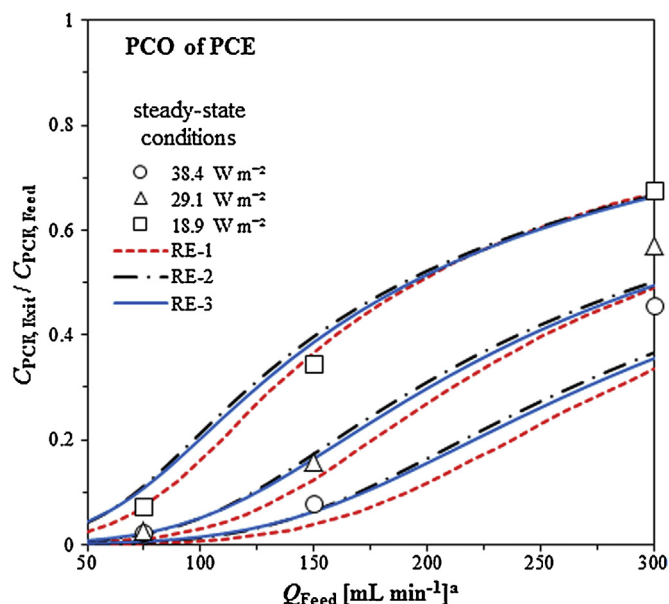
Fig. 6. Effect on PCE degradation through PCO ($C_{PCE,Exit}/C_{PCE,Feed}$, at steady-state conditions) for air contaminated with PCE applying different feed flow rates [Q_{Feed}[a]]: experimental points for incident irradiances measured within 280–400 nm (sunlight UV fraction) of 38.4 ($\bigcirc$), 29.1 ($\triangle$), and 18.9 W m^{-2} ($\square$), and RE-1 (– – –), RE-2 (– · –), and RE-3 (———); $C_{PCE,Feed}$ = 945 ppm, RH_{Feed}[a] = 30%, and T = 298 K; operation conditions reported in Table 2 ([a] measured at 298 K and 1 bar).

3. Results and discussion

3.1. Solar photochemical oxidation of PCE

Blank tests (photoreactor mounted without catalytic bed) were performed in order to establish the effect of direct photolysis on the conversion of PCE. This pollutant is able to absorb light over a wide range of wavelengths but absorption is often stronger at shorter wavelengths (high energy). Because the Pyrex-glass outer
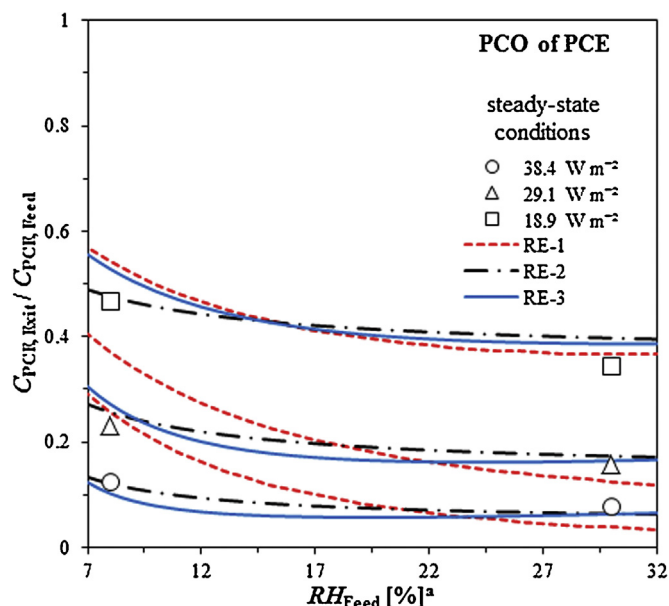

Fig. 7. Effect on PCE degradation through PCO ($C_{PCE,Exit}/C_{PCE,Feed}$, at steady-state conditions) for air feed streams contaminated with different concentrations of PCE [$C_{PCE,Feed}$]: experimental points for incident irradiances measured within 280–400 nm (sunlight UV fraction) of 38.4 ($\bigcirc$), 29.1 ($\triangle$), and 18.9 W m^{-2} ($\square$), and RE-1 (– – –), RE-2 (– · –), and RE-3 (———); Q_{Feed}[a] = 150 mL min^{-1}, RH_{Feed}[a] = 30%, and T = 298 K; operation conditions reported in Table 2 ([a] measured at 298 K and 1 bar).

Fig. 8. Effect on PCE degradation through PCO ($C_{PCE,Exit}/C_{PCE,Feed}$, at steady-state conditions) for air contaminated with PCE applying different humidity contents [RH_{Feed}[a]]: experimental points for incident irradiances measured within 280–400 nm (sunlight UV fraction) of 38.4 ($\bigcirc$), 29.1 ($\triangle$), and 18.9 W m^{-2} ($\square$), and RE-1 (– – –), RE-2 (– · –), and RE-3 (———); Q_{Feed}[a] = 150 mL min^{-1}, $C_{PCE,Feed}$ = 945 ppm, and T = 298 K; operation conditions reported in Table 2 ([a] measured at 298 K and 1 bar).

tube absorbs most of the shorter wavelengths of the simulated solar radiation (for λ < 285 nm), no measurable PCE conversion was detected.

3.2. Solar TiO$_2$-CAM photocatalytic oxidation of PCE

3.2.1. Effect of multi-layered TiO$_2$ coating on PCO of PCE

Multi-layer TiO$_2$ coating was applied on the surface of different cellulose acetate monoliths, resulting in production of three different TiO$_2$-CAM samples (with 3, 6, and 9 dip-coating layers, respectively). By means of continuous pollutant volatilization to ensure an approximately constant PCE-contaminated air stream composition, the PCE concentration in the feed stream was measured in by-pass (via the two-way valves that precede the photoreactor inlet) until steady-state was reached. Then, employing a photoreactor packed with the 3-layered TiO$_2$-CAM sample, the generated gas stream was passed through the catalytic bed in the absence of light (in dark conditions). After the adsorption equilibrium was reached, it was observed that the PCE adsorption capacity on the TiO$_2$ films is ~0.44 mol kg^{-1}.

Using the different multi-layered catalysts, PCE photooxidation experiments under simulated solar irradiation were carried out in the described lab-scale facility (Fig. 1). Tables 1 and 2 report the catalytic bed characteristics and the experimental conditions, respectively. As shown in Fig. 2, the photocatalytic activity was significantly improved when the number of coatings increased from 3 to 9; higher PCE degradation efficiencies were attained for TiO$_2$-CAM with nine dip-coating layers (~92% for an incident irradiance of 38.4 W m^{-2}, measured within 280–400 nm: solar UV fraction). The result achieved suggests that a larger amount of pollutant molecules are adsorbed and oxidized onto the TiO$_2$-CAM with larger number of dip-coating layers. Thus, the results show that as the number of layers increase, so does the number of TiO$_2$ particles deposited during the dip-coating procedure; since the coating thickness is considerably small for all samples, more photogenerated electron–hole pairs are expected because there are more TiO$_2$
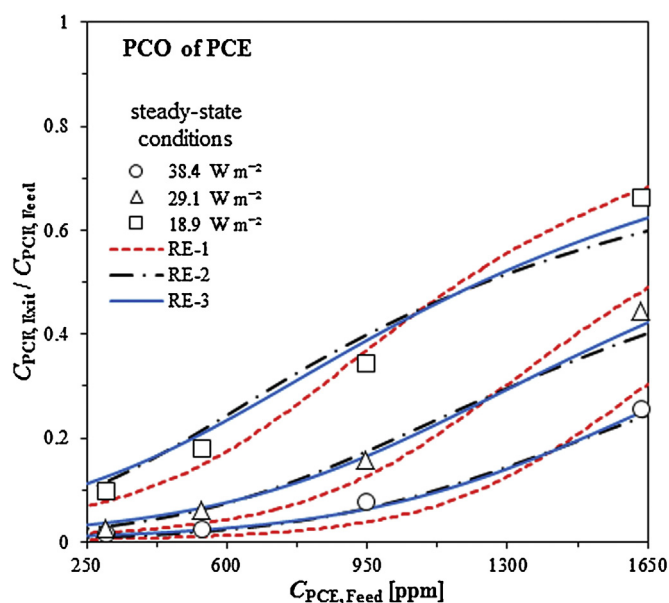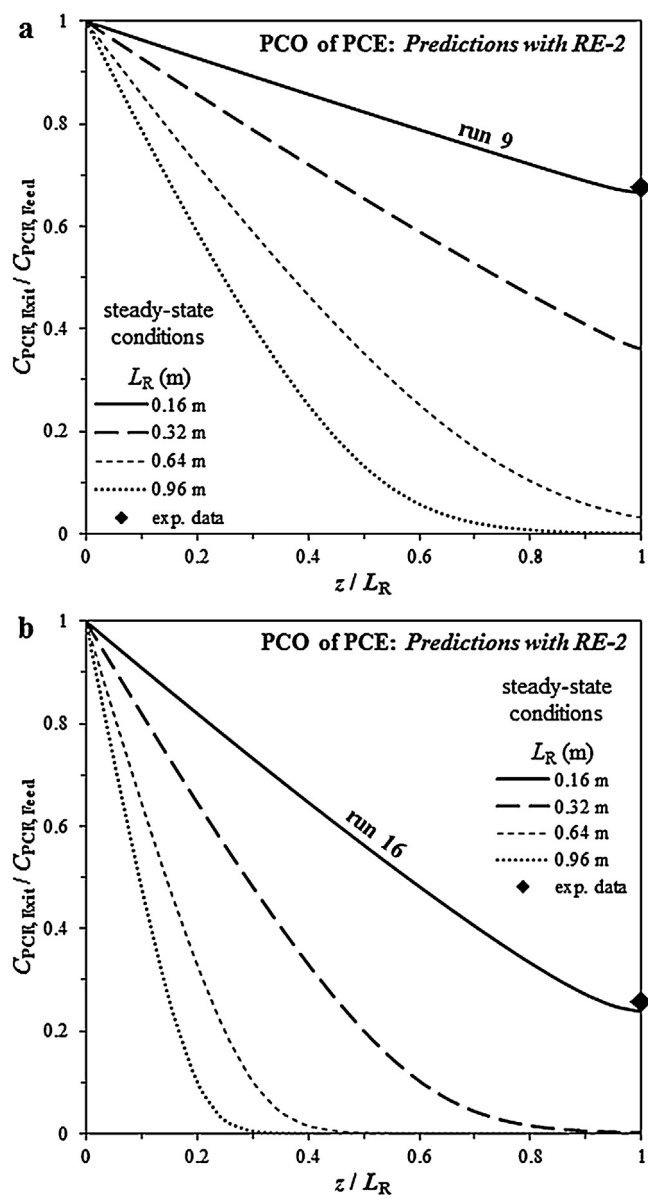
Fig. 9. PCE degradation profiles ($C_{PCE,Exit}/C_{PCE,Feed}$, at steady-state conditions) for photoreactors with different lengths [L_R]: 0.16 (—), 0.32 (– – –), 0.64 (- - -), and 0.96 m (· · ·); (a) C_{Feed} = 945 ppm, Q_{Feed}^a = 300 mL min^{-1}, and I = 18.9 W m^{-2} (measured within 280–400 nm: sunlight UV fraction); (b) $C_{PCE,Feed}$ = 1633 ppm, Q_{Feed}^a = 150 mL min^{-1}, and I = 38.4 W m^{-2} (measured within 280–400 nm: sunlight UV fraction); RH_{Feed}^a = 30%, and T = 298 K; operation conditions reported in Table 2 (runs 9 and 16, respectively) (^{a} measured at 298 K and 1 bar); experimental data (points); mathematical modelling with RE-2 (lines).

particles along the catalyst surface with larger number of layers. However, it should be mentioned that the number of coatings to reach the highest PCE degradation efficiency was not optimized due to the already extremely high degradation efficiencies achieved for the 9-layered TiO$_2$-CAM sample; moreover, increasing the number of depositions does not always lead to higher degradation efficiencies due to the eventual occurrence of "shading effect" [10–12]. There should be a commitment between the number of reproductions of the dip-coating procedure (and their associated cost and time) and the photoactivity of the obtained catalyst sample.

Within this work, the sample presenting highest activity (9-layered TiO$_2$-CAM) was analyzed before and after more than 50 h of photocatalytic operation under simulated solar irradiation and continuous feeding (humid air contaminated with PCE). Fig. 2 shows

not only the results of PCO experiments employing a first use catalyst (full-coloured columns) but also those obtained after 50+ h of use (dotted columns). Results show a slight photocatalytic activity loss (2–5%) after the mentioned exposure time, suggesting that the harsh operational settings employed during more than 50 h resulted in a partial decrease of activity, in line with the results in previous works implementing this type of supports for H$_2$S treatment [9].

By SEM analysis (Fig. 3) was possible to estimate the CAM support thickness (ca. 50 μm; see Fig. 3b), the TiO$_2$ film thickness (ca. 350 nm; see Fig. 3d), and the TiO$_2$ particle size (ca. 7–8 nm; see Fig. 3e), the latter being reported in many works as one optimal size for TiO$_2$ crystallites in photocatalytic studies [20,30,31]. Moreover, Fig. 4 shows the XRD patterns of fresh and used TiO$_2$ powder samples; the 2θ diffraction peaks at 24.8°, 37.4°, 46.9°, 53.1°, 53.7°, and 61.4° correspond to anatase crystalline phase (marked as A in the XRD spectra), the peaks at 25.4°, 25.7°, 30.9°, 36.3°, 48.1°, and 55.3° to brookite crystalline phase (marked as B in the XRD spectra), and the peaks at 27.3°, 35.8°, 41.0°, 54.0°, and 68.6° to rutile crystalline phase (marked as R in the XRD spectra). These three TiO$_2$ crystalline phases were found at similar ratios in both fresh and used samples, with a distribution of 51 (±3), 45 (±3), and 3.5 (±0.5) wt.% of anatase, brookite, and rutile, respectively, and with average crystallite sizes of 5.3, 3.2, and 11 nm.

Fig. 5a and b shows SEM micrographs of the fresh 9-layered TiO$_2$-CAM sample at two different magnifications while Fig. 5b and d shows the respective images of the same sample after 50 h of PCO experiments. According to the SEM images of Fig. 5a and c, the fresh TiO$_2$ film deposited on CAM support show many fissures. These fissures resulted during the preparation method (dry step), probably due to the large difference between the thermal expansion coefficients of the CAM support and the TiO$_2$ film [32]; although less probable, the fissures in the TiO$_2$ film could be generated during the SEM analysis due to the high energy of the incident irradiation. Fig. 5b shows the SEM micrograph of the used sample, at the lower magnification, being observed that some film delamination occurs after the photocatalytic experiments. As observed for the fresh sample (Fig. 5a and c), many fissures were also observed for the used sample (Fig. 5b and d), but in this case these fissures are brighter probably due to the SEM light scattering promoted by the delaminated film or, less probable, due to the partial filling of such fissures with some organics.

Fig. 5e and f shows the results obtained with EDX analysis of both fresh and used sample, respectively. As expected, due to the TiO$_2$ formation, the element map scanning identified Ti and O atoms in both cases. In addition, the identified C atom is related to the adhesive tape for fixing the samples during the SEM imaging while residual P is probably due to some CAM phosphate-containing plasticizer (because these chemicals are the most commonly used flame retardants for cellulose acetate). A certain amount of chlorine associated with Ti and O atoms was also detected in the sample used in PCO of PCE (Fig. 5f), caused by remaining adsorbed PCE and/or any of its photocatalytic reaction intermediates, by-products, and final products [13], and reinforcing the importance of the adsorption process on the photocatalytic degradation of these pollutants.

Therefore, some decline of the film occurs during the long photocatalytic experiments, which seems to be mainly due to the thermal expansion of the CAM support under the employed conditions. However, a high photocatalytic activity was still maintained after the observed deterioration of the TiO$_2$ film, the PCE conversion decreasing only in 2–5% after more than 50 h of operation. In this context, and considering the high photocatalytic efficiency of the 9-layered TiO$_2$-CAM (∼92%), it was decided to test this system in the further experiments of PCO of PCE using simulated solar irradiation.

Table 3
Mathematical model, correlations, boundary conditions, and kinetic rate expressions used for estimation of the kinetic and adsorption equilibrium parameters (and further predictive simulations) of 9-layered TiO_2-CAM photooxidation of PCE under simulated solar irradiation [1,2,12,28,37,38,52–59].

Mathematical model (at steady state conditions)	
Material balance for each component i	$\frac{d}{dz}\left(\varepsilon D_{ax}\frac{dC_i}{dz}\right) - \frac{d}{dz}\left(\bar{u}_{0,ch}C_i\right) - \nu_i r = 0 \quad i = N_2,\ O_2,\ H_2O,\ PCE$

Correlations and parameters	
Axial dispersion (laminar flow)[a,b] [37,38,52]	$D_{ax} = D_m + \frac{1}{192}\frac{\bar{u}_{0,ch}^2 d_{ch}^2}{\varepsilon D_m}$
Superficial velocity (monolithic channels)[c]	$\bar{u}_{0,ch} = Q_{Feed}\left[\pi\left(\frac{1}{2}d_{ot,i}\right)^2 - \pi\left(\frac{1}{2}d_{in,e}\right)^2\right]^{-1}$

	Component i	N_2	O_2	PCE	H_2O
Lennard–Jones parameters [53,54]	σ_i [Å]	3.667	3.106	4.676	2.641
	ε_i/k_B [K]	99.8	43.18	211.1	809.0

Boundary conditions	
Photoreactor feed ($z = 0$)	$C_i\|_{z=0} = C_{i,Feed} \quad i = N_2,\ O_2,\ H_2O,\ PCE$
Photoreactor exit ($z = L_R$)	$\frac{dC_i}{dz}\Big\|_{z=L_R} = 0 \quad i = N_2,\ O_2,\ H_2O,\ PCE$

Kinetic rate expressions	
RE-1 [28,55,56]	$r_{PCE} = I \cdot k\left(\frac{K_{PCE}K_{H_2O}C_{PCE}C_{H_2O}}{(1+K_{PCE}K_{H_2O}C_{PCE}C_{H_2O})^2}\right)$
RE-2 [1,28,55–57]	$r_{PCE} = I \cdot k\left(\frac{K_{PCE}C_{PCE}}{1+K_{PCE}C_{PCE}}\right)\left(\frac{K_{H_2O}C_{H_2O}}{1+K_{H_2O}C_{H_2O}}\right)$
RE-3 [1,2,12,28,55,56,58]	$r_{PCE} = I \cdot k\left(\frac{K_{PCE,1}C_{PCE}}{1+K_{PCE,1}C_{PCE}+K_{H_2O,1}C_{H_2O}}\right)\left(\frac{K_{H_2O,2}C_{H_2O}}{1+K_{PCE,2}C_{PCE}+K_{H_2O,2}C_{H_2O}}\right)$

[a] Molecular diffusivity (D_m in $m^2\,s^{-1}$) for the mixture approximated using the Wilke correlation [59].
[b] Binary molecular diffusivity determined through the Chapman–Enskog equation [54].
[c] Average superficial velocity in the cross-section of each channel of the monolith.

3.2.2. Operating parameters influence on PCO of PCE

Photocatalytic degradation experiments of PCE at different operating conditions were also carried out in the lab-scale facility described in Fig. 1. Under steady-state operation, PCE conversion in PCO ($C_{PCE,Exit}/C_{PCE,Feed}$) was determined as a function of: (1) feed flow rates of 75, 150, and 300 mL min^{-1}, measured at 298 K and 1 bar (Fig. 6; Table 2: runs 1–9); (2) PCE concentrations between 296 and 1633 ppm (Fig. 7; Table 2: runs 1–3 and 10–18); (3) feed relative humidity of 8 and 30%, measured at 298 K and 1 bar (Fig. 8; Table 2: runs 1–3 and 19–21); (4) incident irradiances measured within 280–400 nm (sunlight UV fraction) of 38.4 W m^{-2} (Figs. 6–8; Table 2: runs 1, 4, 7, 10, 13, 16, and 19), 29.1 W m^{-2} (Figs. 6–8; Table 2: runs 2, 5, 8, 11, 14, 17, and 20), and 18.9 W m^{-2} (Figs. 6–8; Table 2: runs 3, 6, 9, 12, 15, 18, and 21). It should be mentioned that, due to the high transmittance of the 9-layered TiO_2-CAM, the incident irradiance was assumed to be constant throughout the axial and radial coordinates the photocatalytic bed.

Higher feed flow rate (Q_{Feed}) corresponds to lower residence time, and so, shorter time to PCE molecules react both with bulk hydroxyl, or chloride radicals and surface electron–hole pairs (see Fig. 6) [28]. Results showed that, a 4-fold reduction of the residence time leads to 1.8, 2.3, and 2.9 times lower degradation efficiencies (Table 2: runs 4 and 7, runs 5 and 8, and runs 6 and 9, respectively). The prepared multi-layered catalysts were also able to achieve high PCE conversions even after employing highly contaminated air streams (see Fig. 7; Table 2: mainly run 16). It is clear that high concentrations will significantly reduce PCE photocatalytic oxidation: the hydroxyl or chloride radicals as well as the electron–hole pairs present in the catalyst surface become no longer sufficient to decompose the large amounts of pollutant molecules. Gas-phase PCO also depends on water vapour content due to continuous consumption of hydroxyl radicals; in addition, competitive adsorption of pollutant and water molecules has also been suggested as an inhibitor of high process efficiencies [2,33]. However, within the

Table 4
Kinetic and adsorption equilibrium parameters resulting from the application of rate expressions RE-1 to RE-3 in the complete mathematical model (see Table 3); statistical parameter squared correlation coefficient (R^2) and sum of squared residuals between experimental and calculated rates (S_R^2).

Rate expression	Parameter	Value	Units	R^2	$S_R^2 \times 10^6$ [mol^2 m^{-4} s^{-2}]
RE-1	k	6.47×10^{-5}	mol m^{-2} s^{-1} W^{-1} m^2	0.961	6.38
	K_{PCE}	78.4	M^{-1}		
	K_{H2O}	1.35×10^{-6}	M^{-1}		
RE-2	k	2.17×10^{-5}	mol m^{-2} s^{-1} W^{-1} m^2	0.975	4.04
	K_{PCE}	120	M^{-1}		
	K_{H_2O}	3.86×10^{-5}	M^{-1}		
RE-3	k	7.46×10^{-4}	mol m^{-2} s^{-1} W^{-1} m^2	0.980	3.62
	$K_{PCE,1}$	297	M^{-1}		
	$K_{H_2O,1}$	1.13×10^{-4}	M^{-1}		
	$K_{PCE,2}$	133	M^{-1}		
	$K_{H_2O,2}$	1.92×10^{-6}	M^{-1}		

Reaction mechanism proposed for the gas-phase photooxidation of PCE under simulated solar irradiation

Scheme 1. Reaction mechanism proposed for the gas-phase TiO_2-CAM PCO of PCE under simulated solar irradiation.
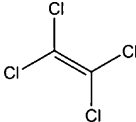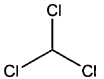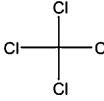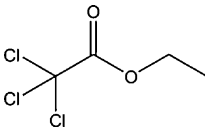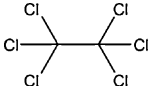
relative humidity range (RH_{Feed}) tested, similar degradation efficiencies were attained under the highest incident irradiation (see Fig. 8; Table 2, runs 1 and 19). Fig. 8 also shows that, when the incident irradiation decreases, the effect of the feed humidity content on the degradation efficiency of PCE becomes more pronounced, i.e., from 4% at incident irradiance with sunlight UV faction of 38.4 W m^{-2} (runs 1 and 19) to 12% at 18.9 W m^{-2} (runs 2 and 21). We can conclude that, less surface electron–hole pairs are available to react with PCE and so more hydroxyl and chloride radicals are needed for PCE conversion.

3.2.3. Modelling of PCO of PCE

A complete mathematical model was developed to estimate the kinetic and equilibrium parameters assuming that the behaviour of the monolith can be fitted to a single channel [34]. In this case, the model is based on one single-square channel ($d_{ch}^2 = 0.009$ m $\times$ 0.009 m, where d_{ch} in m is the characteristic length of the monolithic channel) with a TiO_2 thin coating on the inert wall. An additional simplification was considered: the superficial velocity ($\bar{u}_{0,ch}$ in m s^{-1}) in all the channels is the same. Moreover, the simplified model was employed taking into consideration: (i) steady-state operation; (ii) isothermal and isobaric conditions; (iii) ideal gas behaviour throughout the photocatalytic bed; (iv) axial symmetry; (v) constant porosity; (vi) axial dispersed plug flow through the channel; (vii) no heat transfer resistances and no thermal nor radiation gradients; (viii) no mass, no velocity, and no radiation gradients in the radial direction. At steady-state, dispersion results from both molecular diffusion (in the axial and radial direction) and axial–parallel convection (due to the splitting and recombination of flows throughout the three-dimensional monolithic structure) [35,36]. However, radial diffusion limitations were ignored because $D_m L_R d_{ch}^{-2} \bar{u}_{0,ch}^{-1} \gg 1/56$, where D_m in m^2 s^{-1} is the molecular diffusivity of the feed mixture, and L_R in m is the photoreactor length; this requirement was satisfied within the studied ranges of operational conditions: $200 \geq D_m L_R d_{ch}^{-2} \bar{u}_{0,ch}^{-1} \geq 50$ [36,37].

Table 5
Product analysis by GC/MSD for 9-layered TiO_2-CAM photocatalytic reaction of PCE; experimental conditions described in Table 2 (run 13).

Compound (*i*)	Molecular		CAS no.	C_i [ppm][a]	$C_{i,\text{C-PCE}}$[(a)] [ppm]
	Formula	Structure			
Perchloroethylene[b]	C_2Cl_4		127-18-4	22	3.2
Chloroform	$CHCl_3$		67-66-3	0.79	0.08
Carbon tetrachloride	CCl_4		56-23-5	3.7	0.3
Ethyl trichloroacetate	$C_4H_5Cl_3O_2$		515-84-4	0.41	0.1
Hexachlorethane	C_2Cl_6		67-72-1	1.1	0.1

(a) $C_{i,\text{C-PCE}} = \frac{C_i}{M_i} \cdot (N_{\text{C atom}})|_i \cdot M_{\text{C atom}}$ Mineralization efficiency [%]

$$\eta_{\text{Mineralization}}[\%] = \left[1 - \frac{\sum_i (C_{i,\text{C-PCE}})|_{\text{Exit}}}{\sum_i (C_{i,\text{C-PCE}})|_{\text{Feed}}} \right] \times 100$$

[a] VOC concentration of the major compounds was calculated using the response factor of toluene, except for PCE and trichloroethylene for which specific response factors were used (calibration solutions).
[b] PCE concentration of feed and exit streams were analyzed by MGC: $C_{\text{PCE,Feed}} = 535$ ppm; $C_{\text{C-PCE,Feed}} = 77.5$ ppm.

The mathematical model combined with each suggested rate expression (RE-1 to RE-3 are based on the Langmuir–Hinshelwood (L–H) equation) is described in Table 3. It was solved in gPROMS environment (Process System Enterprise, London, UK), using the orthogonal collocation on finite elements method; 90 elements were used with two interior collocation points (third order polynomials); both absolute and relative tolerance was 1×10^{-5}. The parameter estimation was performed through a sequential quadratic programming algorithm (in gPROMS environment), based on the Newton method for unconstrained optimization (that employs the first order derivative to determine its search direction) [28]. After the parameter estimation (kinetic and adsorption equilibrium parameters reported in Table 4), the complete mathematical model was used for simulating the PCE kinetics of degradation through PCO. All rate expressions employed in modelling can qualitatively describe the experimental PCE degradation data (see Figs. 6–8). However, within the studied ranges of operational conditions, the mathematical model combined with rate expressions RE-2 and RE-3 produce better fit results than when combined with RE-1. Thus, we can conclude that both PCE and H_2O molecules must be considered independent and targeting different active sites of the photocatalyst surface. The surface active sites competition between both molecules can be disregarded: the higher number of parameters required by rate expression RE-3 is less suitable to describe the experimental data.

Once validated the theoretical modelling, there is the possibility of redesign the experimental unit, or even scale-up it into a pilot-scale facility with multiple photocatalytic beds. In this context and using the mathematical model combined with rate expression RE-2, predictive simulations of PCO of PCE were performed for the operational conditions of runs 9 and 16; the PCE degradation profiles reported in Fig. 9 consider different photoreactor lengths (L_R). Fig. 9a shows that, when the highest feed flow rate is employed (run 9), a 2-fold increase of the photoreactors' length yields to a PCE degradation efficiency enhancement of 54%; besides, complete PCE conversion is expected for a single bed reactor with almost 1 m length. According to Fig. 9b, for a photoreactor two times longer than the experimentally employed, only 1% of PCE fed is predictively unreacted (run 16; air stream with the highest pollutant concentration).

3.3. Product analysis and reaction mechanism of PCO of PCE

As previously reported by Petit et al. [4], hydroxyl (HO$^\bullet$) and chloride radicals (Cl$^\bullet$) formation, PCE and its by-products complete mineralization as well as termination reactions are the main steps for the gas-phase photooxidation of PCE under irradiation. Notwithstanding a different opinion published in the literature [33,38], several authors [4,28,39,40] mentioned that the reaction rate coefficient for Cl$^\bullet$ addition to PCE is much higher than for addition of HO$^\bullet$ (without HCl co-feeding, Cl$^\bullet$ formation is the kinetic limiting step). The gas-phase PCE degradation pathways have been suggested in literature [4].

In the present work, identification and quantification of PCE photochemical reaction sub-products was performed through GC/MSD (run 13; operational condition detailed in Table 2). Table 5 shows the by-products of the PCE photocatalytic reaction. According to the identified by-products, and in order to cover all by-products formation, we propose the reaction mechanism described in Scheme 1 for 9-layered TiO_2-CAM PCO of PCE under simulated solar irradiation: mechanism pathways A_1 to E_3 and

intermediates 1 to 5 (in brackets). The suggested reaction mechanism is slightly different than the proposed in our previous work [28]. Despite the most probable formation of trichloroethylene (C_2HCl_3) (pathway A_1), methyl chloroformate ($C_2H_3ClO_2$), butanal (C_4H_8O), chloroacetone (C_3H_5ClO), 1,1-dichloroacetone ($C_3H_4Cl_2O$), methyl trichloroacetate ($C_3H_3Cl_3O_2$), and pentachloroethane (C_2HCl_5), they were not detected as by-product of the photocatalytic reaction. This is essentially due to their reaction (under irradiation) with water, hydroxyl or chloride radicals, or their potential reductive dechlorination, dimerization, and/or C—C bonds cleavage, forming the mineralized final products CO_2, HCl and H_2O. Additionally, PCE can reacts with $Cl^\bullet$ (B_1) forming intermediate 1 (pentachloroethyl radical). If another reaction with a chloride radical occurs (B_2), by-product hexachlorethane (C_2Cl_6) is generated [28,39,41]. However, 1 can also react with O_2 (C_1), generating intermediate 2 (pentachloroethaneperoxyl radical); then, 2 is decomposed into intermediate 3 (pentachloroethoxyl radical) and oxygen, through its dimerization (C_2) [28]. Intermediate 3 covalent carbon—carbon bond (D_1) cleavage can occur under irradiation, generating both 4 (trichloromethyl radical) and CCl_2O (phosgene) [28,33,41–43]. Already published results confirm phosgene as a by-product of PCO of PCE (or trichloroethylene) [44–47]; nonetheless, many other authors indicated in their works that phosgene hydrolysis is promoted in the presence of H_2O (D_2), forming CO_2 and HCl [33,43,48–51]. Intermediate 4 can react with H_2O (D_3) or $Cl^\bullet$ (D_4), leading to the formation of identified by-products chloroform ($CHCl_3$) and carbon tetrachloride (CCl_4), respectively. Regarding intermediate 3 (pentachloroethoxyl radical), the two consecutive $Cl^\bullet$ subtractions in C^1 atom (E_1 followed by E_2) avoid the identification of trichloroacetyl chloride (C_2Cl_4O), directly yielding to intermediate 5 (2,2,2-trichloro-1-oxoethyl radical) formation. In the presence of H_2O, pentachloroethoxyl and 2,2,2-trichloro-1-oxoethyl radicals (intermediates 3 and 5, respectively) can react with each other and, after suffering a reductive dechlorination (E_3), the identified by-product ethyl trichloroacetate ($C_4H_5Cl_3O_2$) and hydroxyl radicals are generated.

Taking into consideration the carbon atoms concentration of each identified by-product formed through PCE degradation (see Table 5), more than 99% of PCE degraded (run 13: ~96% of degradation) were completely mineralized to CO_2, H_2O, and HCl.

4. Conclusions

The gas-phase photooxidation process is an interesting air detoxification technology for the elimination of large amounts of PCE.

The direct photolysis is rather inefficient since leads to a negligible PCE conversion, when the lab-scale continuous-flow tubular photoreactor under simulated solar irradiation is used.

The gas-phase photocatalysis of PCE under simulated sunlight yields to interesting PCE degradation efficiencies of ~92% when using TiO_2-CAM with 9 TiO_2 dip-coating layers. For a 4-fold increase of the feed flow rate, the PCE degradation efficiency drastically drops from 93–98 to 32–54% (depending on the radiation source intensity). High PCE conversions can be attained (80%+) even after feeding the photoreactor with extremely polluted air streams (>1600 ppm of PCE). Under the highest irradiation conditions, similar degradations efficiencies were attained (88–92%) for feed streams with different humidity contents; this parameter becomes more significant for PCO of PCE under radiation sources with lower intensities. Additionally, it was concluded that, despite the good model fittings generally produced by RE-1 to RE-3, the rate expression RE-2 (L–H bimolecular non-competitive two types of sites rate expression) is more suitable to describe the existing data.

Within the most extreme operating conditions (highest feed flow rate, pollutant concentration, and low incident irradiation), some theoretical predictions showed that there is no need to have a photoreactor longer than 1 m to achieve complete degradation of PCE. Products analysis under steady state conditions isolated chloroform, carbon tetrachloride, ethyl trichloroacetate, and hexachlorethane as by-products of the photooxidation reaction of PCE.

The results obtained through GC/MSD showed that the photocatalytic process leads to a 96% of PCE conversion, in which 95% of the PCE fed, is entirely mineralized to CO_2, H_2O, and HCl.

All the experimental data and theoretical modelling validation described in this manuscript allows a simpler and faster unit redesign or its scale-up into multi-bed pilot-facilities able to completely mineralize PCE under solar irradiation.

References

[1] J. Mo, Y. Zhang, Q. Xu, J.J. Lamson, R. Zhao, Atmospheric Environment 43 (2009) 2229–2246.
[2] S. Wang, H.M. Ang, M.O. Tade, Environment International 33 (2007) 694–705.
[3] D.-K. Lee, I.-C. Cho, Microchemical Journal 68 (2001) 215–223.
[4] N. Petit, A. Bouzaza, D. Wolbert, P. Petit, J. Dussaud, Catalysis Today 124 (2007) 266–272.
[5] G.E. Imoberdorf, H.A. Irazoqui, A.E. Cassano, O.M. Alfano, Industrial and Engineering Chemistry Research 44 (2005) 6075–6085.
[6] J.V. Teixeira, S. Miranda, R.A.R. Monteiro, F.V.S. Lopes, J. Madureira, G.V. Silva, N. Pestana, E. Pinto, V.J.P. Vilar, R.A.R. Boaventura, Environmental Monitoring and Assessment (2012), http://dx.doi.org/10.1007/s10661-10012-12533-10660.
[7] M. Hegedűs, A. Dombi, Applied Catalysis B: Environmental 53 (2004) 141–151.
[8] G.E. Imoberdorf, H.A. Irazoqui, O.M. Alfano, A.E. Cassano, Chemical Engineering Science 62 (2007) 793–804.
[9] R. Portela, B. Sánchez, J.M. Coronado, R. Candal, S. Suárez, Catalysis Today 129 (2007) 223–230.
[10] G.E. Imoberdorf, A.E. Cassano, H.A. Irazoqui, O.M. Alfano, Chemical Engineering Science 62 (2007) 1138–1154.
[11] H.T. Chang, N.-M. Wu, F. Zhu, Water Research 34 (2000) 407–416.
[12] T.N. Obee, Environmental Science and Technology 30 (1996) 3578–3584.
[13] B. Sánchez, J.M. Coronado, R. Candal, R. Portela, I. Tejedor, M.A. Anderson, D. Tompkins, T. Lee, Applied Catalysis B: Environmental 66 (2006) 295–301.
[14] P. Avila, A. Bahamonde, J. Blanco, B. Sánchez, A.I. Cardona, M. Romero, Applied Catalysis B: Environmental 17 (1998) 75–88.
[15] A.I. Cardona, R. Candal, B. Sánchez, P. Ávila, M. Rebollar, Energy 29 (2004) 845–852.
[16] Y. Paz, Applied Catalysis B: Environmental 99 (2010) 448–460.
[17] A. Heller, Y. Paz, Y. Haruvy, European Patent Application, EP0844985 A1 (1998).
[18] A. Heller, Y. Paz, Y. Haruvy, European Patent Application, WO97/07069 A1 (1997).
[19] C.B. Greenberg, C.S. Harris, V. Korthuis, L.A. Kutilek, D.E. Singleton, J. Szanyi, J.P. Thiel, PCT International Application, WO98/41480 A1 (1998).
[20] H. Choi, E. Stathatos, D.D. Dionysiou, Applied Catalysis B: Environmental 63 (2006) 60–67.
[21] H. Choi, Novel Preparation of Nanostructured Titanium Dioxide Photocatalytic Particles, Films, Membranes, and Devices for Environmental Applications, Division of Research and Advanced Studies, University of Cincinnati, Cincinnati, OH, 2006.
[22] P. Avila, B. Sanchez, A.I. Cardona, M. Rebollar, R. Candal, Catalysis Today 76 (2002) 271–278.
[23] G.B. Raupp, J.A. Nico, S. Annangi, R. Changrani, R. Annapragada, AIChE Journal 43 (1997) 792–801.
[24] H. Al-Ekabi, N. Serpone, E. Pelizzetti, C. Minero, M.A. Fox, R.B. Draper, Langmuir 5 (1989) 250–255.
[25] B. Sánchez, A.I. Cardona, M. Romero, P. Avila, A. Bahamonde, Catalysis Today 54 (1999) 369–377.

[26] J. Blanco, P. Avila, A. Bahamonde, E. Alvarez, B. Sánchez, M. Romero, Catalysis Today 29 (1996) 437–442.

[27] M.A. Anderson, L.W. Miller, M.I. Tejedor-Anderson, US Patent 6,285,816 B1 (2001).

[28] F.V.S. Lopes, R.A.R. Monteiro, A.M.T. Silva, G.V. Silva, J.L. Faria, A.M. Mendes, V.J.P. Vilar, R.A.R. Boaventura, Chemical Engineering Journal 204–206 (2012) 244–257.

[29] ISO 16000-6, Determination of volatile organic compounds in indoor and test chamber air by active sampling on Tenax TA sorbent, thermal desorption and gas chromatography using MS or MS/FID, 2004.

[30] C.-C. Wang, Z. Zhang, J.Y. Ying, Nanostructured Materials 9 (1997) 583–586.

[31] Z. Zhang, C.-C. Wang, R. Zakaria, J.Y. Ying, Journal of Physical Chemistry B 102 (1998) 10871–10878.

[32] K.N. Rao, Bulletin of Materials Science 26 (2003) 239–245.

[33] S. Yamazaki, H. Tsukamoto, K. Araki, T. Tanimura, I. Tejedor-Tejedor, M.A. Anderson, Applied Catalysis B: Environmental 33 (2001) 109–117.

[34] L.C. Young, B.A. Finlayson, Chemical Reaction Engineering - II, American Chemical Society (1974) 629–643.

[35] D.M. Ruthven, Principal of adsorption and adsorption processes, John Wiley & Sons, New York, 1984.

[36] T. Valdés-Solís, M.J.G. Linders, F. Kapteijn, G. Marbán, A.B. Fuertes, Chemical Engineering Science 59 (2004) 2791–2800.

[37] G.I. Taylor, Proceedings of the Royal Society of London. Series A, Mathematical and Physical Sciences 219 (1953) 186–203.

[38] S. Yamazaki, T. Tanimura, A. Yoshida, K. Hori, Journal of Physical Chemistry A 108 (2004) 5183–5188.

[39] J.M. Nicovich, S. Wang, M.L. McKee, P.H. Wine, Journal of Physical Chemistry 100 (1996) 680–688.

[40] L.P. Thüner, I. Barnes, K.H. Becker, T.J. Wallington, L.K. Christensen, J.J. Orlando, B. Ramacher, Journal of Physical Chemistry A 103 (1999) 8657–8663.

[41] C. Feiyan, S.O. Pehkonen, M.B. Ray, Water Research 36 (2002) 4203–4214.

[42] R.M. Alberici, M.A. Mendes, W.F. Jardim, M.N. Eberlin, Journal of the American Society for Mass Spectrometry 9 (1998) 1321–1327.

[43] S. Yamazaki-Nishida, X. Fu, M.A. Anderson, K. Hori, Journal of Photochemistry and Photobiology A 97 (1996) 175–179.

[44] S. Suárez, N. Arconada, Y. Castro, J.M. Coronado, R. Portela, A. Durán, B. Sánchez, Applied Catalysis B: Environmental 108–109 (2011) 14–21.

[45] S. Suárez, J.M. Coronado, R. Portela, J.C. Martín, M. Yates, P. Avila, B. Sánchez, Environmental Science and Technology 42 (2008) 5892–5896.

[46] M.D. Hernández-Alonso, S. García-Rodríguez, S. Suárez, R. Portela, B. Sánchez, J.M. Coronado, Catalysis Today (2012), http://dx.doi.org/10.1016/j.cattod.2012.01.029.

[47] W.A. Jacoby, M.R. Nimlos, D.M. Blake, R.D. Noble, C.A. Koval, Environmental Science and Technology 28 (1994) 1661–1668.

[48] S. Yamazaki-Nishida, K.J. Nagano, L.A. Phillips, S. Cervera-March, M.A. Anderson, Journal of Photochemistry and Photobiology A 70 (1993) 95–99.

[49] W.A. Zeltner, C.G. Hill Jr., M.A. Anderson, Chemtech 23 (1993) 21–29.

[50] J. Fan, J.T. Yates Jr., Journal of the American Chemical Society 118 (1996) 4686–4692.

[51] P.B. Amama, K. Itoh, M. Murabayashi, Journal of Molecular Catalysis A: Chemical 176 (2001) 165–172.

[52] A. Aris, Proceedings of the Royal Society of London. Series A, Mathematical and Physical Sciences 235 (1956) 67–77.

[53] J. Vrabec, J. Stoll, H. Hasse, Journal of Physical Chemistry B 105 (2001) 12126–12133.

[54] R.B. Bird, W.E. Stewart, E.N. Lightfoot, Transport Phenomena, 2nd ed., Wiley International, Singapore, 2002.

[55] G. Li Puma, I. Salvadó-Estivill, T.N. Obee, S.O. Hay, Separation and Purification Technology 67 (2009) 226–232.

[56] K.-H. Wang, H.-H. Tsai, Y.-H. Hsieh, Applied Catalysis B: Environmental 17 (1998) 313–320.

[57] J. Peral, X. Domènech, D.F. Ollis, Journal of Chemical Technology and Biotechnology 70 (1997) 117–140.

[58] T.N. Obee, R.T. Brown, Environmental Science and Technology 29 (1995) 1223–1231.

[59] C.R. Wilke, Chemical Engineering Progress 46 (1950) 95–104.